



HAL
open science

A New Adaptive Robust Sliding Mode Control for High-Precision PKMs: Design, Stability Analysis, and Experiments

Youcef Mohamed Fitas, Ahmed Chemori, Johann Lamaury, Thierry Roux

► **To cite this version:**

Youcef Mohamed Fitas, Ahmed Chemori, Johann Lamaury, Thierry Roux. A New Adaptive Robust Sliding Mode Control for High-Precision PKMs: Design, Stability Analysis, and Experiments. IEEE Transactions on Automation Science and Engineering, 2024, pp.1-17. 10.1109/TASE.2024.3461156 . lirmm-04713844

HAL Id: lirmm-04713844

<https://hal-lirmm.ccsd.cnrs.fr/lirmm-04713844v1>

Submitted on 30 Sep 2024

HAL is a multi-disciplinary open access archive for the deposit and dissemination of scientific research documents, whether they are published or not. The documents may come from teaching and research institutions in France or abroad, or from public or private research centers.

L'archive ouverte pluridisciplinaire **HAL**, est destinée au dépôt et à la diffusion de documents scientifiques de niveau recherche, publiés ou non, émanant des établissements d'enseignement et de recherche français ou étrangers, des laboratoires publics ou privés.

A New Adaptive Robust Sliding Mode Control for High-Precision PKMs: Design, Stability Analysis, and Experiments

Youcef Fitas, Ahmed Chemori, *Senior Member, IEEE*, Johann Lamaury and Thierry Roux

Abstract—This paper proposes a novel adaptive feedback sliding mode control for parallel kinematic manipulators (PKMs), built on the conventional model-based sliding mode control. This structure was chosen for its robustness towards uncertainties and external disturbances. The contribution of this research is the inclusion of a feedforward term based on the dynamic model of the PKM in the control design. This feedforward term compensates for high nonlinear dynamics, as well as avoids measurement noise in control inputs. Additionally, the fixed feedback gains of the sliding mode controller are redesigned as adaptive gains, which provide better correction actions for larger tracking errors. A stability analysis of the proposed control solution, based on Lyapunov's method, is provided. The effectiveness of the proposed controller is demonstrated through its application to a Gough-Stewart platform (MISTRAL parallel robot) in various real-time experimental scenarios. The proposed controller is compared with both conventional and model-based feedforward sliding mode controllers to demonstrate its superiority. It ensures nominal root mean square tracking errors of (i) about $22 \mu\text{m}$ in joint space, and (ii) about $27 \mu\text{m}$ in traveling plate Cartesian position.

Note to Practitioners — This paper was motivated by the problem of robustness towards uncertainties and operating conditions for PKMs and especially in industry. The literature contains some control solutions to deal with these issues by designing robust or adaptive nonlinear controllers. Indeed, despite their success, for the first type, large uncertainties may degrade the tracking performance and the robustness is not always guaranteed. Adaptive controllers can be more robust, but their tuning can be difficult and especially in the case of real-time estimation of dynamic parameters. In this paper, a new robust-based sliding mode control with adaptive feedback gains is proposed to ensure the robustness towards uncertainties and external disturbances. The idea is to design adaptive feedback gains for a model-based sliding mode control, resulting in an improved robustness, while ensuring an easy tuning of its parameters. The proposed solution is validated through real-time experiments on an industrial parallel robot, and compared with some sliding-mode-based control solutions. The obtained results show clearly the benefits of the proposed control design and its effectiveness as well as robustness. In future work, the proposed controller can be endowed with a real-time estimation of the dynamic parameters, as well as, a redesign based on the super-twisting algorithm.

Index Terms—Sliding mode control, Adaptive control, Stability analysis, Parallel Kinematic Manipulators, Feedforward term, Dynamic model.

Y. Fitas (e-mail: youcef-mohamed.fitas@lirmm.fr), and A. Chemori (e-mail: ahmed.chemori@lirmm.fr) are with LIRMM, University of Montpellier, CNRS, Montpellier, France.

Y. Fitas (e-mail: youcef.fitas@symetrie.fr), J. Lamaury (e-mail: johann.lamaury@symetrie.fr), and T. Roux (e-mail: thierry.roux@symetrie.fr) are with SYMETRIE, Nîmes, France.

I. INTRODUCTION

SINCE the development of robotic systems, many researchers have been exploring their potential application fields. As a result, robots have become increasingly diverse and widely used. Among industrial robots, parallel kinematic manipulators (PKMs) have gained popularity due to their several advantages over serial kinematic manipulators (SKMs) [1]. Various types of PKMs have been designed for industrial applications such as pick and place [2], waste sorting [3], machining [4], [5], dynamic simulation [6] and micro-positioning [7]. PKMs offer several advantages, including high acceleration capabilities, a high payload-to-weight ratio, and high stiffness and precision [1]. However, they are also characterized by highly nonlinear dynamics, several uncertainties and time-varying parameters [8], over-actuation problems (redundant parallel robots) [9], and singularity issues caused by the closed kinematic chain property [10]. As a result, research in this area has gained significant interest these last decades [11], [4], [12].

The research topics related to PKMs include mechanism design [13], modeling [14], trajectory planning [15], and control [16]. This latter, in particular, has gained wide attention from researchers in the robotics community. Various applied control schemes have been designed without using the dynamic model of the robot, relying instead on empirical corrections based on the error signals. These control schemes are commonly known as non-model-based, and include PID-based feedback controllers [17]. While these basic controllers may perform well under nominal operating conditions, they mainly lack robustness, particularly towards high external disturbances or significant uncertainties. To improve their control performances, these schemes are often endowed with fractional order variables. The resulting augmented controller is commonly referred to as fractional order PID controller [18]. Another approach designed to address the lack of robustness in PID-based control is the redesign of its constant gains as nonlinear time-varying ones [19]. Alternatively, other researchers have focused on developing feedback correction by adding new terms, such as the Robust Integral of the Sign of the Error (RISE) feedback control and time-varying RISE feedback control, to improve the robustness with respect to PID control [20], [21].

Besides, new methodologies of non-model-based control schemes have also been proposed by making the controller adaptive. Model Reference Adaptive Control (MRAC) is a popular technique in which the controller adapts to the system

variations and uncertainties, based on a stable reference model response [22]. L1 Adaptive Control has been designed by increasing MRAC control with a state predictor and filtering the control input by a linear low-pass filter [23]. Neural network-based controllers can also be designed as adaptive, using smart control features to adapt to variations and uncertainties [24]. However, these adaptive controllers require a careful tuning of the feedback control parameters, which may be complex and time-consuming.

There are various alternatives to improve the performance with respect to non-model-based controllers for PKMs. One option is to integrate the PKM dynamic model in the control loop as in the computed torque approach, turning the controller into a model-based one [25]. However, this approach has some drawbacks, such as high model dependency and the injection of measurement noise in the control inputs, reducing the tracking performance. To address this issue, a new methodology has been proposed based on the dynamic model as a feedforward term [5], [26]. This term can either be designed as nominal or adaptive, and its goal is to enhance the tracking performance and improve the controller reactivity. In the adaptive case, real-time dynamic parameters estimation has been developed to compensate for their dynamic effects [27] [28]. This type of control scheme can compensate for uncertainties and lead to a significantly improved control performance. In addition to these methods, optimal control schemes, based on the dynamic model, have also been developed. Examples of such schemes include the Linear Quadratic Regulator (LQR) [29], and the Model Predictive Control (MPC) [30]. The MPC determines the control input by optimizing the system's future behavior under certain constraints using a model predictor. This strategy can ensure closed-loop control stability. However, it can be computationally expensive for nonlinear systems [30].

The sliding mode control is a nonlinear robust model-based strategy that can be applied to various types of PKMs [31]. It is able to guarantee robustness against uncertainties and external disturbances by using a signum feedback term. However, this term can lead to a chattering phenomenon, which can be attenuated by using higher-order sliding mode controllers [5], or replacing the linear sliding surface with a nonlinear one. Additionally, terminal sliding mode control can guarantee a finite-time convergence of tracking errors [10]. Sliding mode controllers are most of the time designed for PKMs by integrating their dynamic model in a computed-torque formulation. It is worth noting that the proposed approach in [5] aims to enhance the super-twisting controller by incorporating a feedforward dynamic compensator, in order to address certain limitations associated with the computed-torque formulation. However, the feedback gains in the proposed scheme were designed as constants.

In this paper, a new adaptive sliding mode controller has been developed to improve the tracking performance of the Gough-Stewart Platform for motion simulations. This controller consists of two terms (i) a feedforward term, and (ii) an adaptive sliding mode feedback term. The aim is then to address the limitations of the first-order sliding mode controller while preserving its advantages [31]. In contrast to nonlinear feedback gains, depending on the tracking errors

[26] [25], the ones of the proposed controller are automatically adjusted by an adaptation rule. To this end, the idea here is to achieve enhanced robustness through the real-time adaptation of feedback gains. Additionally, this design demonstrates effectiveness in compensating for inaccuracies in the modeling process and offers easier implementation than model-based adaptive controllers that involve real-time estimation of dynamic parameters. The proposed methodology can be considered as a novel solution for sliding mode control, applied to uncertain nonlinear systems. Furthermore, the proposed controller can be designed for any PKM whose dynamic model takes the general Lagrange form proposed in this paper. To show its effectiveness and robustness, the proposed control scheme has been validated in real-time on a 6-DOF parallel manipulator (MISTRAL robot) in different operating conditions.

The rest of the paper is structured as follows. In Section II, the MISTRAL parallel robot is described in terms of its structure, kinematic model, and dynamic model. Section III presents the proposed control solution, including a detailed formulation of the stability analysis. Section IV presents real-time experimental results for different scenarios. Finally, Section V provides some concluding remarks and the potential future works.

II. ROBOT DESCRIPTION AND MODELING

This section provides a description of the mechanical structure of the MISTRAL parallel robot, followed by a presentation of its kinematic and dynamic models.

A. Description of the MISTRAL Parallel Robot

A Gough-Stewart platform is a parallel manipulator with six degrees of freedom. It consists of six legs formed by prismatic joints, connecting the moving platform to the fixed base through universal joints. The manipulator is actuated by DC motors, generally located at the fixed base [12]. This platform is commonly used as a motion simulator (e.g. for air-crafts, vehicles, boats, tramways, etc.), as well as to test any embedded electronics on ships [32].

MISTRAL is a high-dynamics motion simulation robot, designed based on the non-redundant Gough-Stewart platform cf. illustration of Fig. 1). It provides a 6-DOF motion, with its mobile platform linked to the fixed base through six legs equipped with identical linear actuators, each is composed of a motor and a cylinder. The MISTRAL parallel robot can carry a payload of up to 1 ton and has a maximum height of 2.165 m. It can move its payload at a maximum operational speed of 1 m/s and 100°/s, and a maximum acceleration of 8 m/s² and 800°/s². This allows the MISTRAL parallel robot to reproduce the trajectories of land, naval or air vehicles, making it ideal for laboratory testing of sensors, antennas, and electro-optic systems [11]. All its technical features are available on SYMETRIE website (<https://symetrie.fr/en/hexapods/mistral/>).

B. Kinematics of MISTRAL Parallel Robot

Let the 6-dimensional coordinate vector $X = [x \ y \ z \ \phi \ \theta \ \psi]^T \in \mathbb{R}^6$ denotes the position and orientation

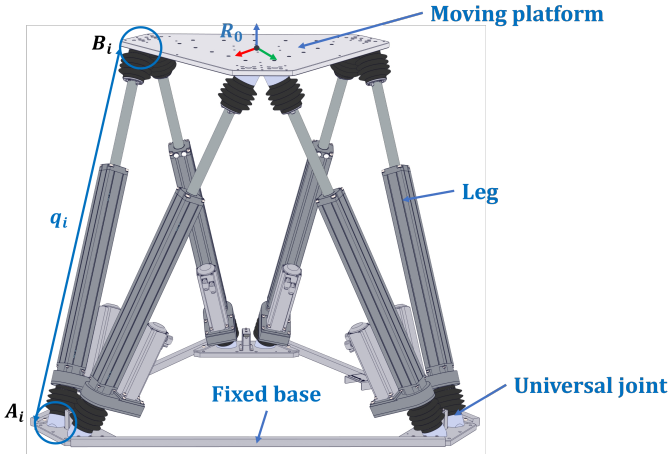


Fig. 1. CAD-View of MISTRAL parallel robot with its main components.

of the moving platform in the operational reference frame R_0 (cf. Fig. 1), and the 6-dimensional coordinate vector $q = [q_1 \cdots q_6]^T \in \mathbb{R}^6$ denotes the prismatic joints as the lengths of the six legs. They are attached to the fixed base at six points. Let $A_i, i = \overline{1,6}$ denote the position coordinate vectors of these points in the reference frame R_0 . At the moving platform side, $B_i, i = \overline{1,6}$ represents the position coordinate vectors of the attachment points of the legs in the moving platform reference frame. The inverse kinematic model expresses the joint vector q based on the knowledge of the Cartesian coordinate vector X ($q = IK(X)$) [33]. This relationship is given by the following equation:

$$q_i = \|P + RB_i - A_i\|, i = \overline{1,6} \quad (1)$$

where $P = [xyz]^T \in \mathbb{R}^3$ is the position of the moving platform in the R_0 reference frame. $R \in \mathbb{R}^{3 \times 3}$ is the rotation matrix of the moving platform. The symbol $\|\cdot\|$ denotes the standard Euclidean norm. In order to develop the dynamic model of the robot, the differential kinematic model is also necessary for the conversion between the joint and the Cartesian spaces [33]. For that the prismatic joint velocity vector \dot{q} is expressed as follows:

$$\dot{q} = J\dot{X} \quad (2)$$

where $\dot{X} \in \mathbb{R}^6$ is the Cartesian velocity vector, and $J \in \mathbb{R}^{6 \times 6}$ is the Jacobian matrix given by

$$J = \begin{bmatrix} S_1^T & (RB_1 \wedge S_1)^T \\ \vdots & \vdots \\ S_6^T & (RB_6 \wedge S_6)^T \end{bmatrix}. \quad (3)$$

The symbol \wedge denotes the cross product of two vectors, and $S_i \in \mathbb{R}^3, i = \overline{1,6}$ is the nominal vector of the robot's i th leg length vector, expressed by

$$S_i = \frac{P + RB_i - A_i}{q_i}, i = \overline{1,6}. \quad (4)$$

For further details about the kinematics of the Gough-Stewart platform, the reader is referred to [12].

C. Dynamic Model of MISTRAL Parallel Robot

The MISTRAL parallel robot undergoes dynamic analysis in both joint and operational spaces, resulting in a general dynamic model. This latter is developed using the Lagrange formulation, and obtained by summing up the two resulting dynamic equations [33]. For a better implementation efficiency, it can be simplified by considering the following assumptions:

- **Assumption 1:** The elastic phenomena at the cylinders and the moving platform are neglected due to their limited effect.
- **Assumption 2:** The dry and viscous frictions are neglected for all passive joints, thanks to an appropriate design. Only active joints ones are considered.

The total resulting force acting on the moving platform comprises (i) inertial forces, (ii) Coriolis and centrifugal forces, and (iii) gravity force as follows:

$$F_p = M_p(X)\ddot{X} + C_p(X, \dot{X})\dot{X} + G_p(X) \quad (5)$$

where $M_p(X) \in \mathbb{R}^{6 \times 6}$ is the moving platform mass matrix, $C_p(X, \dot{X}) \in \mathbb{R}^{6 \times 6}$ is its Coriolis and centrifugal matrix, $G_p(X) \in \mathbb{R}^6$ is its gravity vector, and $\ddot{X} \in \mathbb{R}^6$ is the Cartesian acceleration vector. These dynamic terms are expressed as follows:

$$M_p(X) = \begin{bmatrix} m_p I_3 & -m_p D \\ m_p D & RI_p R^T - m_p DD \end{bmatrix} \quad (6)$$

$$C_p(X, \dot{X}) = \begin{bmatrix} 0_{3 \times 3} & -m_p QD \\ 0_{3 \times 3} & -Q(RI_p R^T - m_p DD) \end{bmatrix} \quad (7)$$

$$G_p(X) = \begin{bmatrix} m_p V_g \\ m_p V_g \wedge -Rd \end{bmatrix} \quad (8)$$

where m_p is the moving platform mass, $I_p \in \mathbb{R}^{3 \times 3}$ is its inertia matrix, $D \in \mathbb{R}^{3 \times 3}$ and $Q \in \mathbb{R}^{3 \times 3}$ are the cross-product matrix of the moving platform center of mass and its rotation angles matrices, respectively, $d \in \mathbb{R}^3$ is the moving platform center of mass coordinate vector, and $V_g = [00g]^T \in \mathbb{R}^3$ is the gravitational acceleration vector, where g is the gravitational constant. Note that, $I_3 \in \mathbb{R}^{3 \times 3}$ is the 3×3 identity matrix. The torque contributions of this resulting force are obtained using the Jacobian matrix J , as follows:

$$\Gamma_p = k_f J^T (M_p(X)\ddot{X} + C_p(X, \dot{X})\dot{X} + G_p(X)) \quad (9)$$

where k_f is the conversion coefficient between the force applied by the leg and the motor torque. In the joint space, the legs' torque vector is given by:

$$\Gamma_m = k_f (k_\alpha I_M \ddot{q} + F_v \dot{q} + F_s \text{sign}(\dot{q})) \quad (10)$$

where $\ddot{q} \in \mathbb{R}^6$ is the joint acceleration vector, $I_M = I_m I_6$ is the actuator equivalent inertia matrix at the motor level, $F_v = f_v I_6$ and $F_s = f_s I_6$ are the viscous and dry friction coefficient matrices, respectively. Note that $I_6 \in \mathbb{R}^{6 \times 6}$ is the 6×6 identity matrix. Finally k_α is the conversion coefficient between the leg length and the motor angular position. Then, the MISTRAL inverse dynamic model can be expressed as:

$$\Gamma_p + \Gamma_m = \Gamma \quad (11)$$

TABLE I
SUMMARY OF MISTRAL PARALLEL ROBOT DYNAMIC PARAMETERS

Parameter	Description	Value
m_p	Moving platform mass	93.2 Kg
I_x	x axis moving platform inertia	9.96 Kg.m ²
I_y	y axis moving platform inertia	9.96 Kg.m ²
I_z	z axis moving platform inertia	19.61 Kg.m ²
I_m	Actuator inertia	0.000507 Kg.m ²
f_v	Viscous friction coefficient	0.7009 N.s/m
f_s	Dry friction coefficient	95.4602 N

where $\Gamma \in \mathbb{R}^6$ is the control input torque vector. By using the Jacobian matrix J , this dynamic model can be rewritten in the joint space as follows:

$$M(q)\ddot{q} + C(q, \dot{q})\dot{q} + G(q) + \Gamma_f(\dot{q}) = \Gamma \quad (12)$$

where:

$$M(q) = k_f \left(J^{T^{-1}} M_p(X) J^{-1} + k_\alpha I_M \right), \quad (13)$$

$$C(q, \dot{q}) = k_f J^{T^{-1}} \left(M_p(X) J^{-1} \dot{J} J^{-1} - C_p(X, \dot{X}) \right), \quad (14)$$

$$G(q) = k_f J^{T^{-1}} G_p(X), \quad (15)$$

$$\Gamma_f(\dot{q}) = k_f (F_v \dot{q} + F_s \text{sign}(\dot{q})). \quad (16)$$

TABLE I summarizes the dynamic parameters of the MISTRAL parallel robot, determined using various procedures. The mass of the moving platform was measured experimentally, while its inertia matrix was calculated using the SolidWorks CAD software. The actuators' dynamic parameters are obtained through an experimental identification procedure [34]. The identification procedure begins by selecting the vector of dynamic parameters to be identified, as well as the resulting regressor matrix, both of which are derived from the dynamic model. Subsequently, a database is generated, containing the applied torques and the corresponding regressor values. This database is compiled through the execution of high-acceleration trajectories. Finally, the identified values are obtained using quadratic optimization techniques [35].

Note that the mass matrix $M(q) \in \mathbb{R}^{6 \times 6}$ is symmetric positive definite, satisfying:

$$m_{\min} \|\zeta\|^2 \leq \zeta^T M(q) \zeta \leq m_{\max}(q) \|\zeta\|^2, \forall \zeta \in \mathbb{R}^6 \quad (17)$$

where m_{\min} is a positive constant and $m_{\max}(q) \in \mathbb{R}$ is a positive non-decreasing function.

III. PROPOSED CONTROL SOLUTION

In this section, the proposed control solution for the MISTRAL parallel robot is detailed.

A. Motivation and background

The Sliding Mode Control (SMC) is a nonlinear robust controller with a fast transient response, developed to ensure robustness in the presence of external disturbances and uncertainties [36]. Its main property is to ensure the convergence in finite time of the sliding surface, regardless of the operating conditions, especially in the case of significant uncertainties,

without the need for system identification. As a result, it guarantees an asymptotic convergence of the tracking errors [31], and this steady-state is ensured even in the presence of bounded disturbances, making it an ideal controller for uncertain nonlinear systems [31]. In the case of first-order sliding mode control, the sliding surface is defined as a linear combination of e and \dot{e} , the position and velocity tracking errors, respectively, as follows:

$$s = \dot{e} + \lambda e \quad (18)$$

with

$$e = q_d - q \quad (19)$$

where $q_d \in \mathbb{R}^6$ is the vector of the desired joint positions and λ is a positive constant. For SMC, the control law contains continuous and discrete components [31], as follows:

$$\Gamma = \Gamma_c + M(q)\Gamma_{SMC} \quad (20)$$

where Γ_c is the continuous time control term, and $\Gamma_{SMC} = K \text{sign}(s)$ is the switching control term which ensures the system convergence i.e., $s^T \dot{s} < 0$. [36] Then, the sliding mode control law for the parallel manipulators is given by:

$$\Gamma = M(q)(\ddot{q}_d + \lambda \dot{e} + K \text{sign}(s)) + C(q, \dot{q})\dot{q} + G(q) + \Gamma_f(\dot{q}) \quad (21)$$

where $K \in \mathbb{R}^{6 \times 6}$ is a diagonal positive-definite matrix [31].

The first-order sliding mode control has some drawbacks, such as a chattering phenomenon caused by the presence of the sign feedback term [36]. Although this term guarantees stability in the presence of uncertainties and external disturbances, it injects noise into the control signal due to the combined error sign changes. Additionally, poor control performances may occur in the presence of significant uncertainties, caused by the computed torque formulation [5]. Indeed, it may result in a false compensation for large uncertainties in the mass matrix $M(q)$, ultimately leading to a degradation in control performance. Furthermore, since the computed torque formulation is based on the measured joint lengths to compute the dynamics, the controller may be more sensitive to measurement noise, which may potentially degrade the tracking performance [5].

To make this controller less sensitive to measurement noise, the dependent term of the measured joint positions can be replaced with the desired joint positions' idem. This approach involves redesigning the computed torque term as a feed-forward one, which can improve the tracking performance by eliminating measurement noise and canceling high nonlinearities [37]. Moreover, this term can be computed offline, reducing thereby computation time during real-time execution [38]. Our study also proposes to redesign the constant feedback gain matrices to be adaptive in order to achieve better tracking performance, especially in the case of time-varying dynamic parameters and uncertainties [39]. The new proposed design will provide a better corrective action when the combined errors increase significantly, by increasing the feedback gain values [39]. This solution makes the controller more robust in the presence of large uncertainties and easier to tune, compared to adaptive controllers based on real-time

estimation of dynamic parameters [23]. Consequently, there is no need to estimate uncertainties. These advantages make the proposed controller a good solution for improving tracking performance, especially in the presence of uncertainties and hard non-linearities.

B. Proposed controller: Adaptive Feedback Sliding Mode Controller (AFbSMC)

The proposed controller is based on two terms, namely (i) the nominal feedforward term, and (ii) the adaptive sliding mode feedback term, as follows:

$$\Gamma = \Gamma_{ff} + \Gamma_{A-SMC} \quad (22)$$

where Γ_{ff} is the nominal feedforward term, and Γ_{A-SMC} is the adaptive sliding mode feedback term. The former is based on the dynamic model of the robot (12), and is given as follows:

$$\Gamma_{ff} = M(q_d)\ddot{q}_d + C(q_d, \dot{q}_d)\dot{q}_d + G(q_d) + \Gamma_f(\dot{q}_d) \quad (23)$$

The latter is given by:

$$\Gamma_{A-SMC} = K(t)s + K_s(t)\text{sign}(s) \quad (24)$$

where $K(t) \in \mathbb{R}^{6 \times 6}$, and $K_s(t) \in \mathbb{R}^{6 \times 6}$ are diagonal positive-definite matrices. These feedback gain matrices are designed adaptive. Note that the sliding surface is defined in (18). The first feedback term in (22) is linear with respect to the combined errors. The objective is to insure the asymptotic convergence of the resulting closed-loop system [36]. The feedback gain matrices $K(t)$, and $K_s(t)$ are expressed as follows:

$$K(t) = \Delta_1 \nu + K_1 \quad (25)$$

$$K_s(t) = \Delta_2 \nu + K_2 \quad (26)$$

where $\Delta_1, \Delta_2, K_1, K_2 \in \mathbb{R}^{6 \times 6}$ are diagonal positive-definite matrices and $\nu \in \mathbb{R}^{6 \times 6}$ is the nonlinear adaptation function. The new proposed design involves increasing the minimum threshold to provide a better correction. The additional feedback correction is dependent on Δ_1 and Δ_2 [39], as well as the term ν , representing the dynamics of the adaptive gains. This term must depend on the tracking errors in order to compensate for significant errors and their offsets from zero [39]. Additionally, it must be positive to provide additional feedback action in the case of large tracking errors. To this end, ν is designed as follows:

$$\nu = \text{diag}(|\sigma|) \quad (27)$$

where $\sigma \in \mathbb{R}^6$ is a nonlinear function. The adaptation rule for σ is given by:

$$\tau \dot{\sigma} = \text{sign}(s) - \sigma \quad (28)$$

where $\tau > 0$ is the adaptation gain. The term σ is the response of a first-order system where the input is the sign of the combined error. This adaptation law ensures that σ will increase or decrease depending on the combined error sign [40]. As a result, the feedback gains provide a better correction for large tracking errors. It should be noted that the function σ is bounded, which helps to limit the overshoots on the control

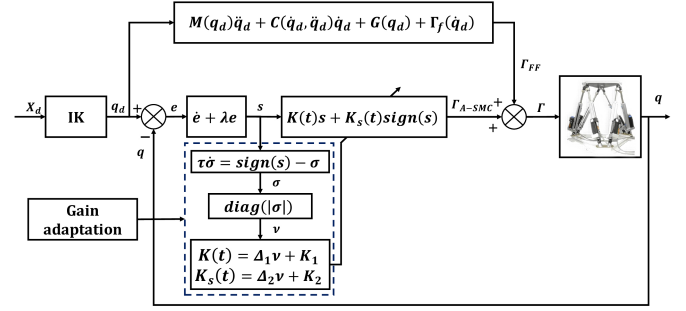


Fig. 2. Block diagram of the proposed control solution.

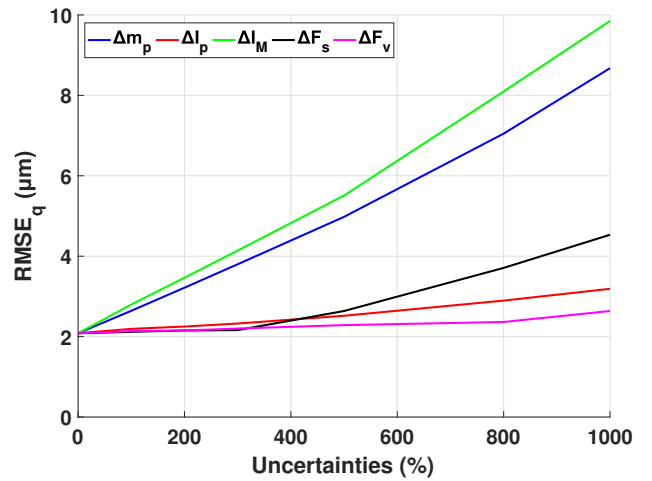


Fig. 3. Illustration of the proposed control solution sensitivity with respect to uncertainties on the robot dynamic parameters (numerical simulation).

inputs. The usefulness of τ is to control the adaptation speed [40], as it represents the time constant for the system given by equation (28). The block diagram of the proposed control solution is illustrated in Fig. 2. In numerical simulation, a sensitivity study of the proposed controller is conducted with respect to uncertainties on the robot's dynamic parameters, as illustrated in Fig. 3. This figure displays the evolution of the root mean square joint errors versus uncertainties. This result shows clearly that the proposed controller is more sensitive to the platform mass and the actuator's equivalent inertia than the other dynamic parameters.

C. Closed-loop stability analysis

The objective of this section is to analyze the stability of the resulting closed-loop system based on the proposed control solution.

Theorem 1: The tracking errors in joint space of any PKM (e.g. delta robot, planar parallel robot, Gough-Stewart platform, CDPs, etc) whose dynamics is governed by the general form (12), under the control law (22), converge exponentially

to the origin, provided that the parameters γ and Σ_b are designed such that:

$$\begin{aligned} i) \quad & \gamma > \frac{1 - \|\sigma\|}{\tau [(\Upsilon_{\alpha b}\|s\| + \Upsilon_{\beta b})\|s\| - \Sigma_b]} \\ ii) \quad & \Sigma_b < (\Upsilon_{\alpha b}\|s\| + \Upsilon_{\beta b})\|s\| \end{aligned}$$

Proof of Theorem 1: Considering the robot dynamic model developed in (12), the sliding variable defined in (18), and the proposed control law in (22), the sliding surface dynamics can be written as follows:

$$M(q)\dot{s} = -\Gamma_{A-SMC} - h(q, \dot{q}) - C(q, \dot{q})\dot{e} + \lambda M(q)\dot{e} \quad (29)$$

where $h(q, \dot{q})$ being the residual dynamics expressed as follows:

$$h(q, \dot{q}) = [M(q_d) - M(q)]\ddot{q}_d + [C(q_d, \dot{q}_d) - C(q, \dot{q})]\dot{q}_d + [G(q_d) + \Gamma_f(\dot{q}_d) - G(q) + \Gamma_f(\dot{q})] \quad (30)$$

It is worth noting that the Euclidean norm of the residual dynamics can be upper bounded as follows:

$$\|h(q, \dot{q})\| \leq K_{h_1}\|\dot{e}\| + K_{h_2}\|e\| \quad (31)$$

where K_{h_1} and K_{h_2} are two positive constants [41]. Thus, the sliding variable time-derivative can be expressed as follows:

$$\dot{s} = \Psi + \Upsilon_{\alpha} \nu s + \Upsilon_{\beta} \nu \text{sign}(s) \quad (32)$$

where Ψ, Υ_{α} and Υ_{β} are nonlinear functions, defined as follows:

$$\begin{aligned} \Psi &= \lambda \dot{e} - \\ M(q)^{-1} (K_1 s + K_2 \text{sign}(s) + h(q, \dot{q}) + C(q, \dot{q})\dot{e}) \end{aligned} \quad (33)$$

$$\Upsilon_{\alpha} = -M(q)^{-1} \Delta_1 \quad (34)$$

$$\Upsilon_{\beta} = -M(q)^{-1} \Delta_2 \quad (35)$$

For the stability analysis of the resulting closed-loop system, let us consider the following positive definite, radially unbounded, Lipschitz continuous Lyapunov candidate function:

$$V(s, \sigma) = \frac{1}{2} s^T s + \frac{1}{2\gamma} \sigma^T \sigma \quad (36)$$

where $\gamma > 0$ is a positive gain to be designed. Note that $V(s, \sigma)$ satisfies the following condition:

$$V_m \left[\|s\|^2 + \frac{\|\sigma\|^2}{\gamma} \right] \leq V(s, \sigma) \leq V_M \left[\|s\|^2 + \frac{\|\sigma\|^2}{\gamma} \right] \quad (37)$$

where V_m and V_M are two positive constants. The time-derivative of the Lyapunov function is given by:

$$\dot{V}(s, \sigma) = s^T \dot{s} + \frac{1}{\gamma} \sigma^T \dot{\sigma} \quad (38)$$

Replacing the time-derivative of the sliding variable (32) in (38) leads to:

$$\dot{V}(s, \sigma) = s^T (\Psi + \Upsilon_{\alpha} \nu s + \Upsilon_{\beta} \nu \text{sign}(s)) + \frac{1}{\gamma} \sigma^T \dot{\sigma} \quad (39)$$

Based on the upper bound of the residual dynamics (31) and the mass matrix property (17), the time-derivative of the Lyapunov function can be upper-bounded as follows:

$$\begin{aligned} \dot{V}(s, \sigma) &\leq -(\Psi_b + \Upsilon_{\alpha b}\|\nu\|\|s\| + \Upsilon_{\beta b}\|\nu\|)\|s\| \\ &\quad + \frac{1}{\gamma\tau} \sigma^T (\text{sign}(s) - \sigma) \end{aligned} \quad (40)$$

where $\Psi_b, \Upsilon_{\alpha b}$ and $\Upsilon_{\beta b}$ are positive constants. By introducing $\Sigma_b > 0$, the time-derivative can be upper-bounded as follows:

$$\begin{aligned} \dot{V}(s, \sigma) &\leq -(\Psi_b + \Upsilon_{\alpha b}\|\nu\|\|s\| + \Upsilon_{\beta b}\|\nu\|)\|s\| \\ &\quad + \frac{1}{\gamma\tau} (\|\sigma\| - \|\sigma\|^2) + \Sigma_b\|\sigma\| - \Sigma_b\|\sigma\| \end{aligned} \quad (41)$$

where $\|\nu\| = \sqrt{\text{tr}(\nu^T \nu)} = \|\sigma\|$. The inequality (41) can be rewritten as:

$$\dot{V}(s, \sigma) \leq -\Psi_b\|s\| - \Sigma_b\|\sigma\| - \rho \quad (42)$$

where ρ is given as:

$$\rho = \|\sigma\| \left[\Upsilon_{\alpha b}\|s\| + \Upsilon_{\beta b}\|s\| - \Sigma_b - \frac{1}{\gamma\tau} (1 - \|\sigma\|) \right] \quad (43)$$

By choosing γ in order to ensure $\rho > 0$, the expression (42) can be rewritten as follows:

$$\dot{V}(s, \sigma) \leq -\Sigma V(s, \sigma)^{\frac{1}{2}} \quad (44)$$

where $\Sigma = \min \{ \Psi_b \sqrt{2}, \Sigma_b \sqrt{2\gamma} \}$ and γ respects the following inequality:

$$\gamma > \frac{1 - \|\sigma\|}{\tau [(\Upsilon_{\alpha b}\|s\| + \Upsilon_{\beta b})\|s\| - \Sigma_b]} \quad (45)$$

where Σ_b is selected as:

$$\Sigma_b < (\Upsilon_{\alpha b}\|s\| + \Upsilon_{\beta b})\|s\| \quad (46)$$

Furthermore, $\|\sigma\| \leq 1$ because σ_i for $i = \overline{1, 6}$ is the response of a stable BIBO (bounded input bounded output) first order system $G(s) = \frac{1}{\tau s + 1}$ with bounded input $\|u_i\| = \|\text{sign}(s_i)\| \leq 1, \forall i = \overline{1, 6}$. This implies that $V(s, \sigma)$ is exponentially stable and $\|s\|$ converges exponentially in finite-time to the set $S = \{s \in \mathbb{R}^6, \|s\| \leq \epsilon\}$ for all $\epsilon > 0$ from any initial condition $\|s(0)\| > \epsilon$. Consequently, the tracking errors converge exponentially to the origin.

IV. REAL-TIME EXPERIMENTAL RESULTS

This section presents the obtained real-time experimental results discussed to demonstrate the effectiveness and superiority of the proposed control solution. A comparative study between the proposed controller (AFbSMC) and the original SMC [31] is conducted to achieve this objective. Since their structures are different, another comparative study with the following feedforward sliding mode controller (FFSMC), where the feedback gains are designed constants, is also considered:

$$\Gamma_{FFSMC} = \Gamma_{ff} + Ks + K_s \text{sign}(s) \quad (47)$$

The experimental validation includes the following scenarios:



Fig. 4. Illustration of the experimental setup configurations for robustness tests, towards inertia changes (on the left), and payload changes (on the right).

- **Scenario 1 – Nominal case:** The three controllers are compared under nominal conditions without uncertainties and external disturbances.
- **Scenario 2 – Robustness towards payload changes:** In this case (cf. illustration of Fig.4) different payloads are progressively fixed on the robot’s moving platform for robustness test purposes. First, an empty 184 Kg sandbox is considered. Next, a 296 Kg sandbag is added, resulting in a total payload of 480 Kg. Finally, another 438 Kg sandbag is added, resulting in a total payload of 918 Kg. It is worth noting that the control nominal design does not consider these added payloads, and all the control design parameters are kept the same as the nominal scenario to demonstrate the robustness of the proposed control scheme.
- **Scenario 3 – Robustness towards inertia changes:** In this scenario (cf. illustration of Fig.4), the objective is to test the controller’s robustness towards inertia changes, while the payload being carried remains the same. To achieve this, a 400 Kg iron plate is first attached to the platform, then a mass of 150 Kg is added and fixed at the diagonal extremity of the traveling plate. To properly shift the center of mass, the payload added to the iron plate is then doubled. The purpose of this test is to assess the controller’s ability to handle changes in the distribution of the mass and thereby inertia of the moving platform, without considering the payload mass, and its center in the control law.
- **Scenario 4 – Robustness towards dynamics variations:** The robustness of the proposed controller can also be tested towards variations in the motion velocities and accelerations. To this end, three high-dynamic tests have been conducted. It is worth noting that, in this scenario, no payload has been considered.

A. Description of the experimental setup

The MISTRAL 800-P parallel robot, described in section II-A, is equipped with high-dynamics brushless DC motors and absolute EnDat 2.2 encoders with a resolution of 2^{20} counts per revolution. The motors can produce a maximum torque of 18 N.m and a maximum speed of 3500 rpm. The encoders’ data are read to measure the motor’s angular positions, which

are used to calculate the corresponding prismatic joint lengths (the resulting resolution is greater than 10^5 counts per millimeter). To control these motors, six servo drives are used, receiving Cyclic Synchronous Torque (CST) commands from the controller at a servo cycle of 2 kHz through an EtherCAT fieldbus. For the servo control, an OMRON CK3E controller, including a 2-core ARMv7I CPU with a clock frequency of 1 GHz, is used. This servo control is performed in joint space using the joint length feedback.

The designed control schemes are first implemented using Matlab/Simulink software from MathWorks. Then, the block diagram is converted to a C-language code to be uploaded into the CK3E controller using the PPMAC IDE, provided by OMRON company. In the case of the conventional sliding mode controller, the Cartesian coordinates of the moving platform, used in a computed torque model-based formulation, are determined by solving the forward kinematic problem. In contrast, for the proposed controller, the Cartesian coordinates are directly obtained from the desired trajectories, and then the feedforward term is injected into the control loop. Furthermore, if the tracking errors exceed their maximum authorized values for safety, the robot is programmed to halt its operation. Notably, the conventional SMC experienced fault errors in scenarios 2 and 3 when dealing with payloads of 918 Kg and 700 Kg, respectively. To avoid overshoots in the input torques during the motion, the sign function was replaced by a smooth approximation based on the hyperbolic tangent function. This modification is proposed to eliminate any discontinuities in the control signal.

The desired trajectories are sent to the CK3E controller using the SYM_Motion software developed by SYMETRIE. This software serves as the main interface to control SYMETRIE Hexapods and enables multiple movement type creation, validation, and execution. Additionally, it ensures a continuous communication with the CK3E controller through the TCP/IP Ethernet connection protocol.

B. Desired trajectories generation and evaluation criteria

The desired trajectories were designed and validated using SYM_Motion software. Consequently, they respect the robot’s workspace constraints and avoid singularities. Additionally, the different control and movement variables should not exceed their maximum values, whether at the level of the motors, the legs, or the moving platform. For the first three scenarios, the moving platform orientations $[\phi \ \theta \ \psi]$ were designed as sinusoidal reference trajectories with an amplitude of 3° and a frequency of 0.25 Hz. It is worth noting that, there is a 120° phase shift between the different rotation angles. For the translations, a 3D-view of the Cartesian desired trajectory is illustrated in Fig. 6. The moving platform rises from point A to point B and then starts a spiral movement while moving upwards until the point C, covering a broad range of the operational workspace. It then moves to the origin of a horizontal plane at $z = 0.1 \text{ m}$ (point D) before returning back to point A. The trajectory has a total time of 30 seconds and is repeated twice.

For the last scenario, a circular-shaped trajectory with respect to the horizontal plane was developed. The circle

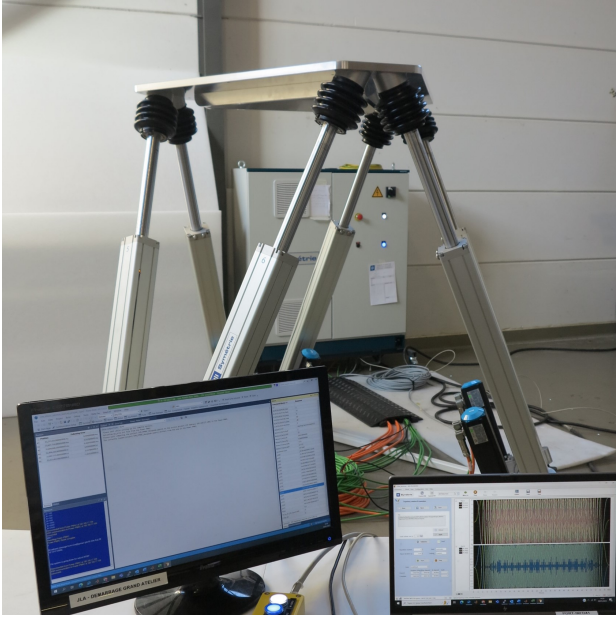


Fig. 5. View of the experimental setup of MISTRAL parallel robot.

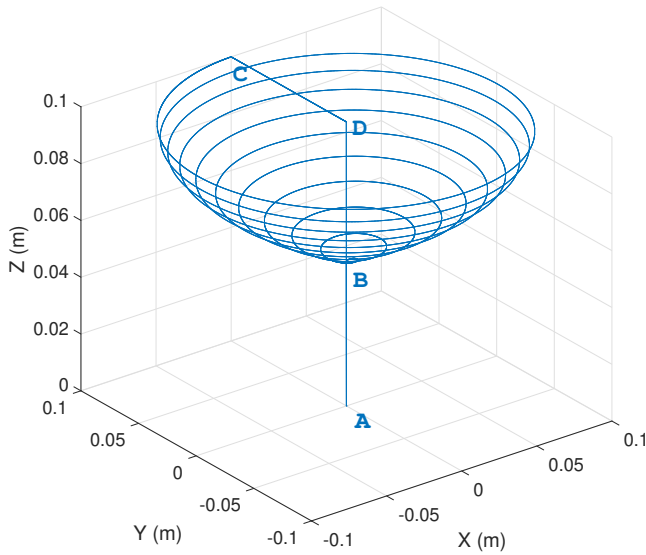


Fig. 6. 3D-View of the desired Cartesian trajectory (for the first three scenarios).

center is located at $(x_0 = 0, y_0 = 0)$, and has a radius of $r = 0.01\text{ m}$. The circular trajectory frequency is set to $f_1 = 1\text{ Hz}$ for the first test, to $f_2 = 1.4\text{ Hz}$ for the second one, and to $f_3 = 1.6\text{ Hz}$ for the third one. The reference trajectory for the vertical movement of the platform is sinusoidal with an amplitude of $z_m = 0.01\text{ m}$ and a frequency equals to half of the circular trajectory frequency. To sum up, a 3D-view of the desired Cartesian trajectory for the fourth scenario is illustrated in Fig. 7. The rotation variables $[\phi \ \theta \ \psi]$ reference trajectories are also sinusoidal with an amplitude of 2° and a frequency

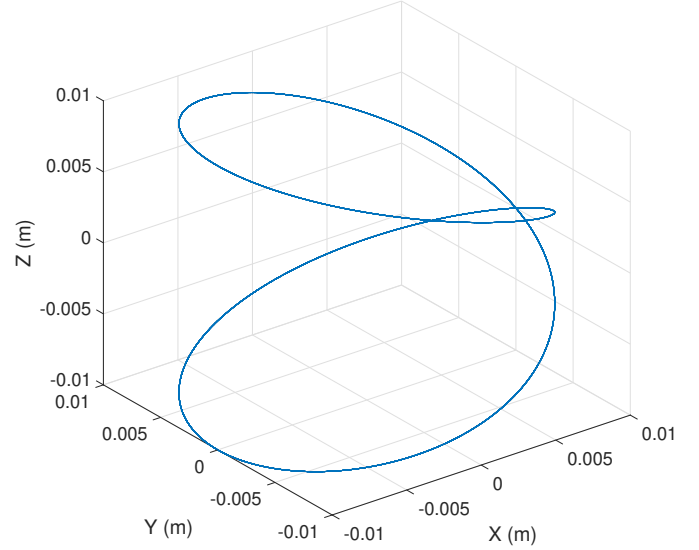


Fig. 7. 3D-View of the desired Cartesian trajectory (for the fourth scenario).

TABLE II
THE JOINT MAXIMUM VELOCITY AND ACCELERATION VALUES FOR HIGH DYNAMICS ROBUSTNESS CASE

Test	Maximum joint velocity	Maximum joint acceleration
Test 1	0.35 m/s	2.35 m/s^2
Test 2	0.46 m/s	4.55 m/s^2
Test 3	0.53 m/s	6 m/s^2

equal to the circular trajectory frequency. The 120° phase shift between the rotation angles is always respected. The total time of this trajectory is equal to 60 seconds. The objective behind this design is to achieve high dynamics with strong velocities and accelerations in the joint space, as summarized in TABLE II.

To compare the tracking performance of the designed controllers, root mean square error (RMSE-based) evaluation criteria are used. They provide a good numerical basis for the comparative analysis. Specifically, the RMSE of the moving platform translation $RMSE_t$, of its rotation $RMSE_r$, and of the joint lengths $RMSE_q$ are defined as follows:

$$RMSE_t = \sqrt{\frac{1}{N} \sum_{i=1}^N (e_x^2(i) + e_y^2(i) + e_z^2(i))} \quad (48)$$

$$RMSE_r = \sqrt{\frac{1}{N} \sum_{i=1}^N (e_\phi^2(i) + e_\theta^2(i) + e_\psi^2(i))} \quad (49)$$

$$RMSE_q = \sqrt{\frac{1}{N} \sum_{i=1}^N \left(\sum_{j=1}^6 e_{q_j}^2(i) \right)} \quad (50)$$

where $e_x, e_y, e_z, e_\phi, e_\theta$ and e_ψ are the Cartesian tracking errors, $e_{q_j}, j = \overline{1, 6}$ are the joint tracking errors and N is the total number of samples.

C. Proposed parameters tuning algorithm

The parameters of the proposed Adaptive Feedback Sliding Mode Controller (AFbSMC) are tuned using an iterative trial-and-error approach. After several adjustment attempts, it is concluded that the optimal values for the controller's parameters can be obtained through the following algorithm:

Control parameters tuning algorithm

- 1) Initialization $K_1 = I_6$, $K_2 = 0$, $\lambda = I_6$, $\Delta_1 = 0$, $\Delta_2 = 0$, and $\tau = 1$.
- 2) Step response control (In numerical simulation).
 - Increase or decrease λ until obtaining a stable response.
 - Increase or decrease K_1 to obtain good control performances.
- 3) Parabolic motion control.
 - Increase K_2 with simultaneously adjusting K_1 to obtain acceptable tracking performances.
 - Increase Δ_1 and Δ_2 to obtain the best possible control performances. Take care of the chattering and the high-frequency vibrations. If one of the two phenomena appears, adjust also K_1 and K_2 . The objective is to find an upper bound for $K_1 + \Delta_1$ and $K_2 + \Delta_2$.
 - Adjust again K_1 and K_2 to improve the tracking performances, if possible.
 - Finally, adjust τ in order to control the adaptation speed. The objective is to improve the feedback correction smoothness, as well as attenuate the potential vibrations and overshoots in the control inputs.

The obtained results of this tuning for the proposed controller (AFbSMC), along with the control design parameters of the original SMC and the FFSMC controllers are summarized in TABLE III.

TABLE III
SUMMARY OF THE CONTROL DESIGN PARAMETERS

SMC	FFSMC	AFbSMC
$\lambda = 30I_6$	$\lambda = 175I_6$	$\lambda = 180I_6$
$K = 1.4I_6$	$K = 136I_6$	$K_1 = 136I_6$
	$K_s = 5.1I_6$	$K_2 = 5.1I_6$
		$\Delta_1 = 22.8I_6$
		$\Delta_2 = 1.14I_6$
		$\tau = 0.1I_6$

D. Obtained experimental results

Scenario 1: Nominal case: The joint tracking errors are plotted in Fig. 8. The plot is zoomed in within the range of [12s, 18s] for better visual clarity. These errors are improved by the proposed controller, compared to the original SMC. The tracking performance of the proposed controller and the FFSMC controller are close with a slightly better performance for the proposed controller. The Cartesian tracking errors are depicted in Fig. 9 between 12s and 18s, to clearly show the difference. The original SMC exhibits a larger tracking error in the z-axis and in the rotations. Notably, the proposed controller improves the tracking performance, compared to the FFSMC

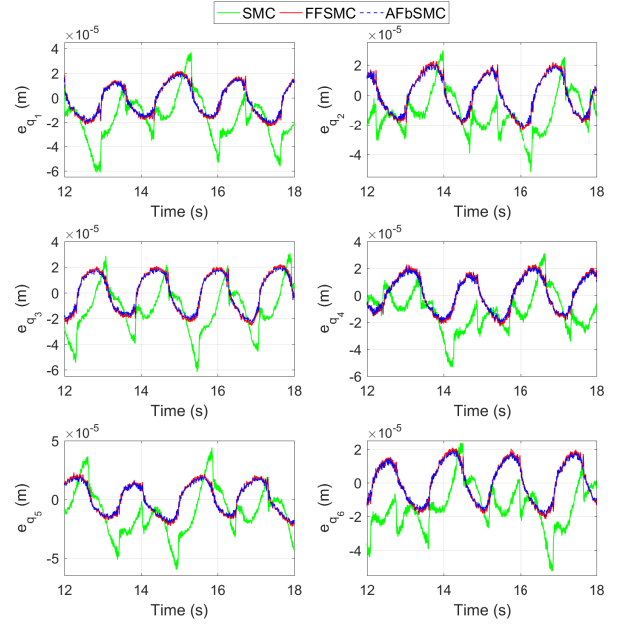


Fig. 8. Scenario 1: Evolution of the joint tracking errors versus time.

TABLE IV
SCENARIO 1: TRACKING PERFORMANCE EVALUATION

Controllers	$RMSE_q (\mu m)$	$RMSE_t (\mu m)$	$RMSE_r (mdeg)$
SMC	56.4492	28.8913	2.4508
FFSMC	24.7453	28.3588	0.9740
AFbSMC	22.9166	26.4969	0.8157
Imp./SMC	59.40 %	08.28 %	66.71 %
Imp./FFSMC	07.39 %	06.56 %	16.25 %

controller, thanks to the online adaptation of the feedback gains. These gains are plotted in Figs. 10 and 11. The evolution of the control inputs versus time is depicted in Fig. 12 and zoomed in within the range [19s, 21s] for better visual clarity. As expected, the control torques do not exceed their maximum values. However, the conventional SMC controller produces more noisy signals due to joint length measurement feedback. The energy consumption of the three controllers is almost the same. TABLE IV summarizes the RMSE performance indices for all the three controllers, while pointing out the improvements of the proposed AFbSMC scheme with respect to the other controllers.

Scenario 2: Robustness towards payload changes: Because the feedforward term and the model-based compensation of the conventional SMC are nominal and can not efficiently account for additional payloads, a large static error appears for the joint lengths and height. This offset is caused by the gravity effect and is clearly noticeable in Fig. 13 and in the z-axis of Fig. 14. For these figures, the plot is zoomed in within the range [12s, 18s] to better highlight the difference between the controllers. Thanks to its adaptive gains, depicted in Figs. 15 and 16, the proposed controller improves the tracking performance, compared to the other control strategies. Additionally, it can lessen the gravity effect on the tracking

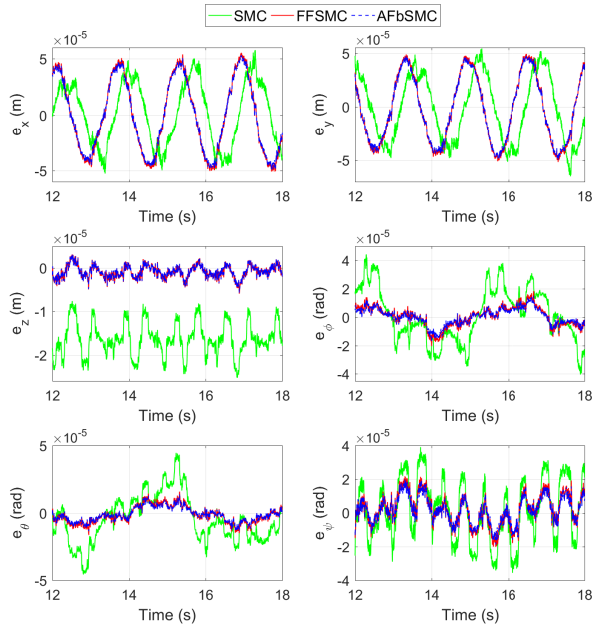


Fig. 9. Scenario 1: Evolution of the Cartesian tracking errors versus time.

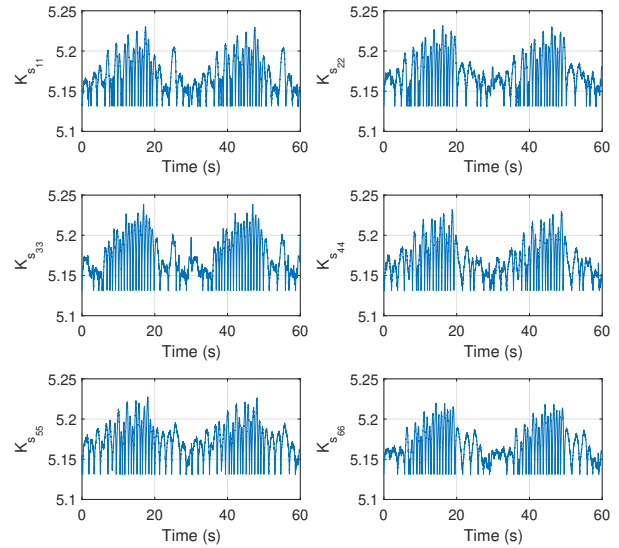


Fig. 11. Scenario 1: Evolution of the sign feedback gains versus time.

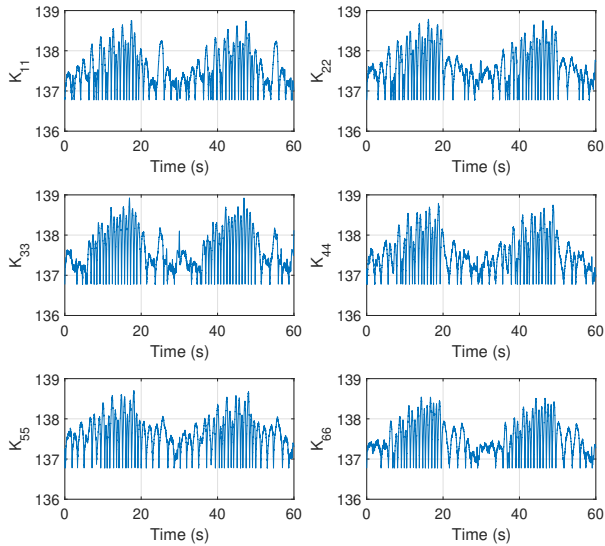


Fig. 10. Scenario 1: Evolution of the linear feedback gains versus time.

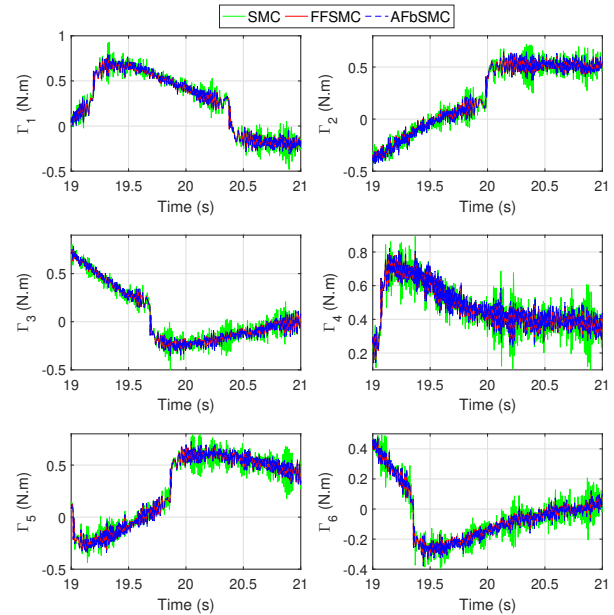


Fig. 12. Scenario 1: Evolution of the input torques versus time.

errors, which is more evident in the rotational motion (cf. Fig. 14). The motor control inputs are plotted in Fig. 17, between 19s and 21s, with the plot zoomed in for better visibility and clarity. The energy consumed by the three controllers is almost the same, and all the generated torques remain within their admissible limits. However, the overall consumed energy is greater than in the nominal case, due to the additional payload. TABLES V, VI, and VII summarize the RMSE performance indices in this scenario, with a 184 Kg, 480 Kg, and 918 Kg payloads, respectively. A sensitivity of the proposed controller

with respect to the moving platform mass uncertainties is depicted in Fig. 18. The proposed controller guarantees robustness in terms of performance up to 200 % of payload mass uncertainties.

Scenario 3: Robustness towards inertia changes: The joint tracking errors are depicted in Fig. 19, within the range [12s, 18s] for a better visual clarity. In a similar way as the previous case, the payload-induced gravity effect causes a significant state error in the joint lengths. This latter is also present in the rotation angles ϕ and θ and height, as the

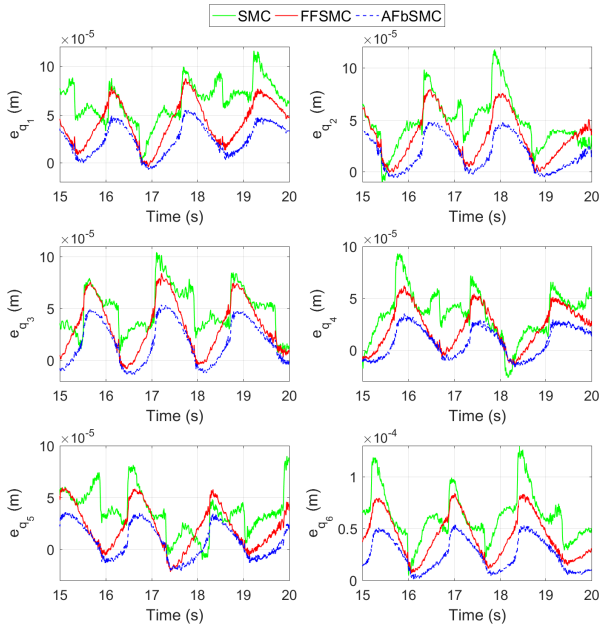


Fig. 13. Scenario 2 (480 Kg payload): Evolution of the joint tracking errors versus time.

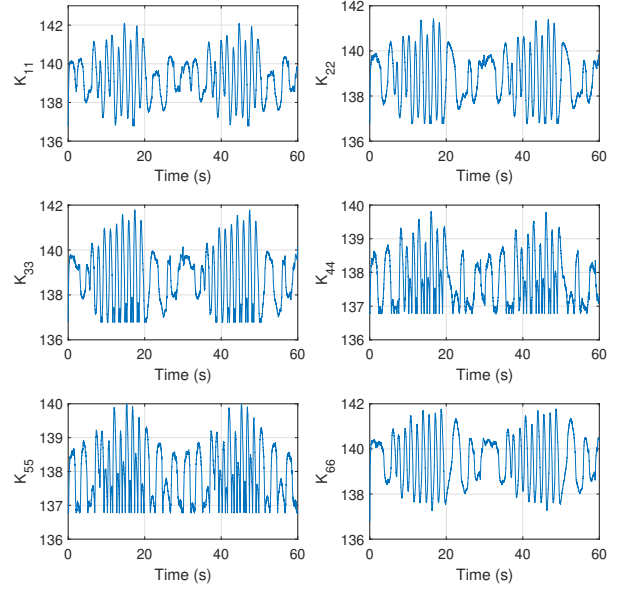


Fig. 15. Scenario 2 (480 Kg payload): Evolution of the linear feedback gains versus time.

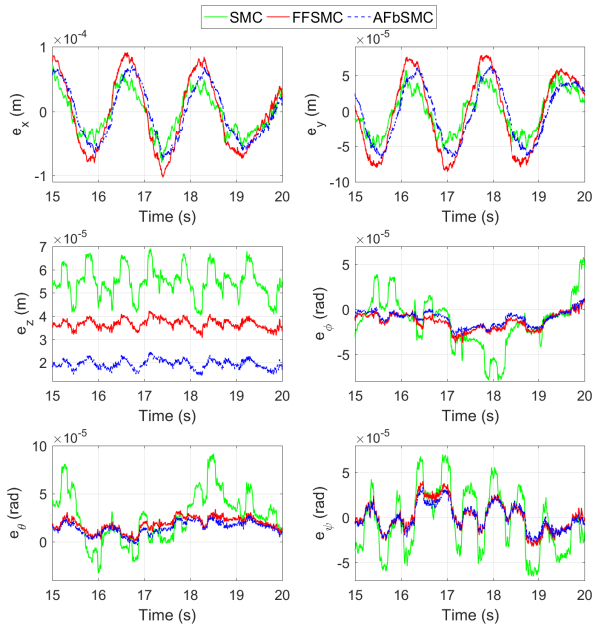


Fig. 14. Scenario 2 (480 Kg payload): Evolution of the Cartesian tracking errors versus time.

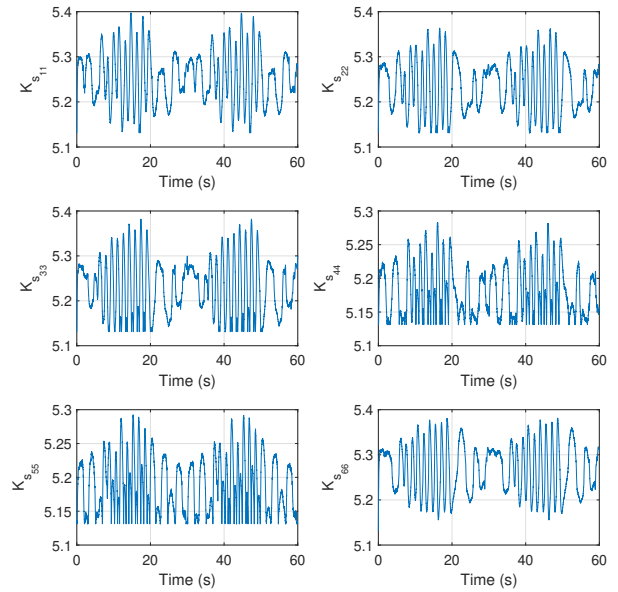


Fig. 16. Scenario 2 (480 Kg payload): Evolution of the sign feedback gains versus time.

TABLE V
SCENARIO 2 (184 KG PAYLOAD): TRACKING PERFORMANCE EVALUATION

Controllers	$RMSE_q(\mu m)$	$RMSE_t(\mu m)$	$RMSE_r(mdeg)$
SMC	64.8531	31.0067	3.3725
FFSMC	30.5219	29.5116	1.0441
AFbSMC	24.8998	27.2352	0.8491
Imp./SMC	61.60 %	12.16 %	74.82 %
Imp./FFSMC	18.42 %	07.71 %	18.67 %

TABLE VI
SCENARIO 2 (480 KG PAYLOAD): TRACKING PERFORMANCE EVALUATION

Controllers	$RMSE_q(\mu m)$	$RMSE_t(\mu m)$	$RMSE_r(mdeg)$
SMC	144.6361	66.0904	4.3480
FFSMC	92.4476	58.3414	1.9083
AFbSMC	55.4726	41.3828	1.4640
Imp./SMC	61.64 %	37.38 %	66.33 %
Imp./FFSMC	39.99 %	29.06 %	23.28 %

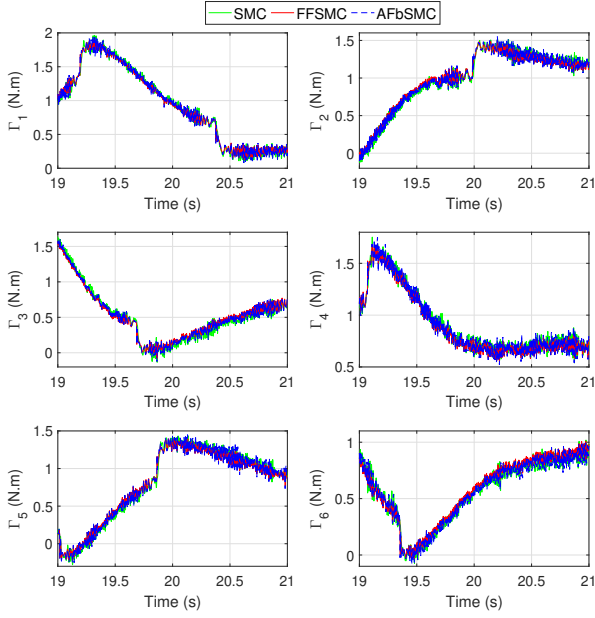


Fig. 17. Scenario 2 (480 Kg payload): Evolution of the input torques versus time.

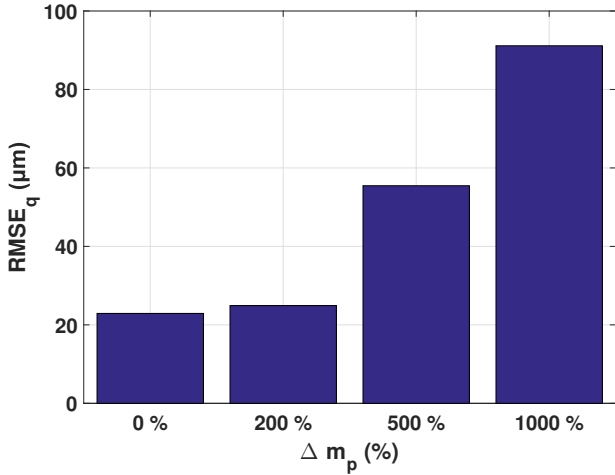


Fig. 18. Scenario 2: Evolution of the $RMSE_q$ versus mass uncertainty Δm_p in %.

TABLE VII
SCENARIO 2 (918 KG PAYLOAD): TRACKING PERFORMANCE EVALUATION

Controllers	$RMSE_q(\mu m)$	$RMSE_t(\mu m)$	$RMSE_r(mdeg)$
FFSMC	163.3601	91.9661	1.9754
AFbSMC	91.1432	62.7195	1.5907
Imp./FFSMC	44.20 %	31.80 %	19.47 %

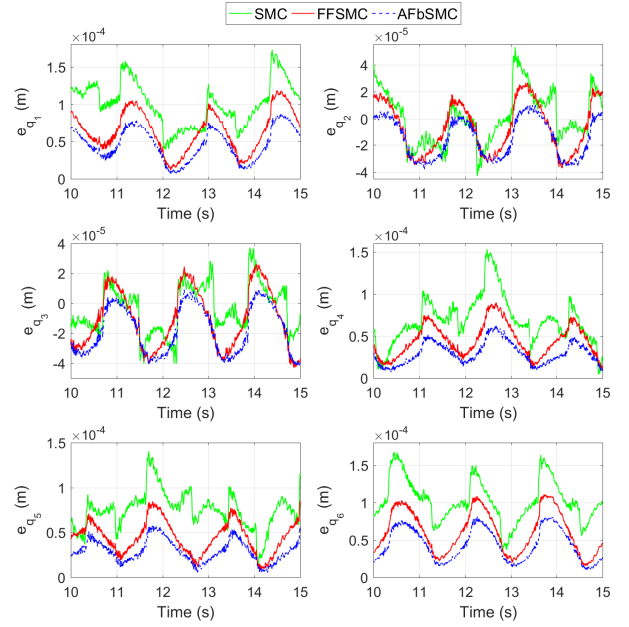


Fig. 19. Scenario 3 (550 Kg payload): Evolution of the joint tracking errors versus time.

TABLE VIII
SCENARIO 3 (550 KG PAYLOAD): TRACKING PERFORMANCE EVALUATION

Controllers	$RMSE_q(\mu m)$	$RMSE_t(\mu m)$	$RMSE_r(mdeg)$
SMC	190.0708	75.2197	7.3799
FFSMC	117.0238	64.8967	4.9597
AFbSMC	85.6212	44.3123	4.0369
Imp./SMC	54.95 %	41.09 %	45.29 %
Imp./FFSMC	26.83 %	31.71 %	18.60 %

payload's center of mass is away from the central vertical line of the moving platform. The Cartesian tracking errors, displayed in Fig. 20 within the range $[12, 18s]$ for a readability purpose, reveal this result. The proposed controller ensures robustness, thanks to its design as well as its adaptive feedback gains, depicted in Figs. 21 and 22. The motor control inputs are shown in Fig. 23, where the plot is also zoomed in within the range $[19s, 21s]$ to better highlight the difference between the controllers. As in previous cases, all the generated torques remain within their admissible range. However, some motors experience higher torque values due to the payload fixing position. In terms of energy consumption, the controllers require almost similar amounts of energy. The proposed AFbSMC improvements also demonstrate its effectiveness in the case of robustness towards inertia changes through the obtained RMSE values summarized in TABLES VIII and IX. As the previous case, a sensitivity study of the proposed controller with respect to the moving platform inertia uncertainties is displayed in Fig. 24. This study demonstrates the ability of the proposed solution to guarantee the robustness towards uncertainties and dynamic model inaccuracies.

Scenario 4: Robustness towards dynamics variations: The evolution of the joint tracking errors is plotted in Fig.

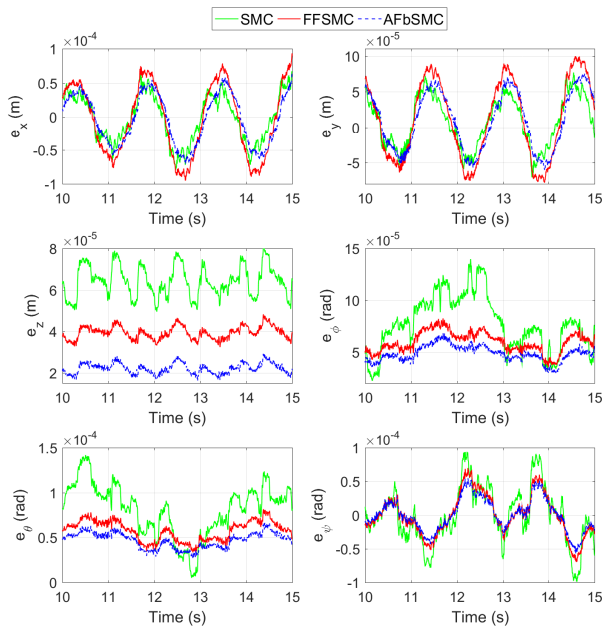


Fig. 20. Scenario 3 (550 Kg payload): Evolution of the Cartesian tracking errors versus time.

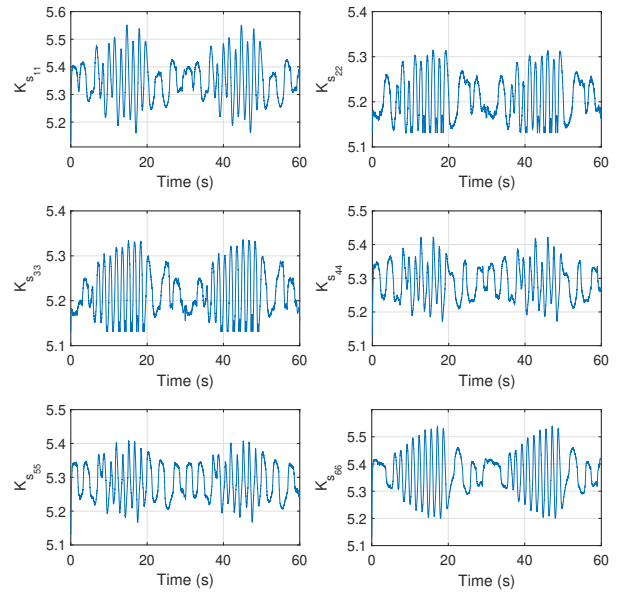


Fig. 22. Scenario 3 (550 Kg payload): Evolution of the sign feedback gains versus time.

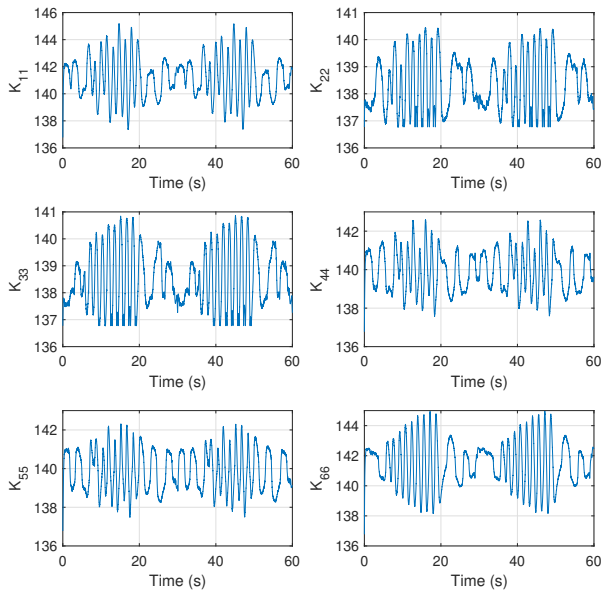


Fig. 21. Scenario 3 (550 Kg payload): Evolution of the linear feedback gains versus time.

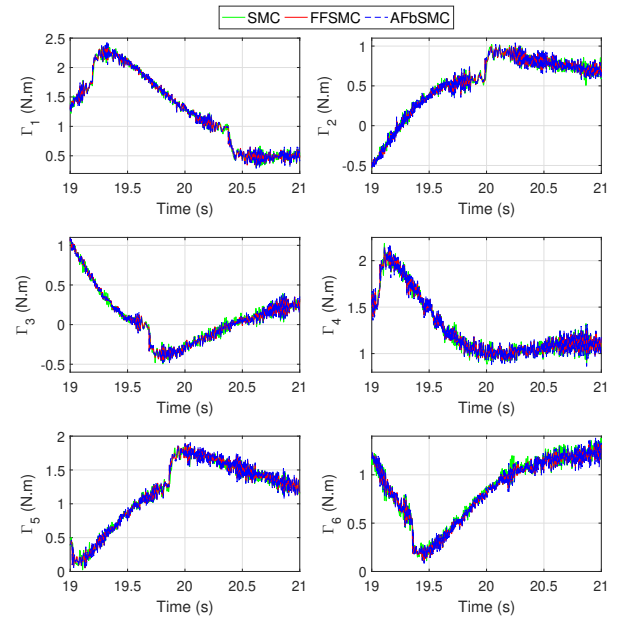


Fig. 23. Scenario 3 (550 Kg payload): Evolution of the input torques versus time.

TABLE IX

SCENARIO 3 (700 KG PAYLOAD): TRACKING PERFORMANCE EVALUATION

Controllers	$RMSE_q(\mu m)$	$RMSE_t(\mu m)$	$RMSE_r(mdeg)$
FFSMC	210.7872	100.0720	9.8104
AFbSMC	156.2284	63.8812	7.8621
Imp./FFSMC	25.88 %	36.16 %	19.85 %

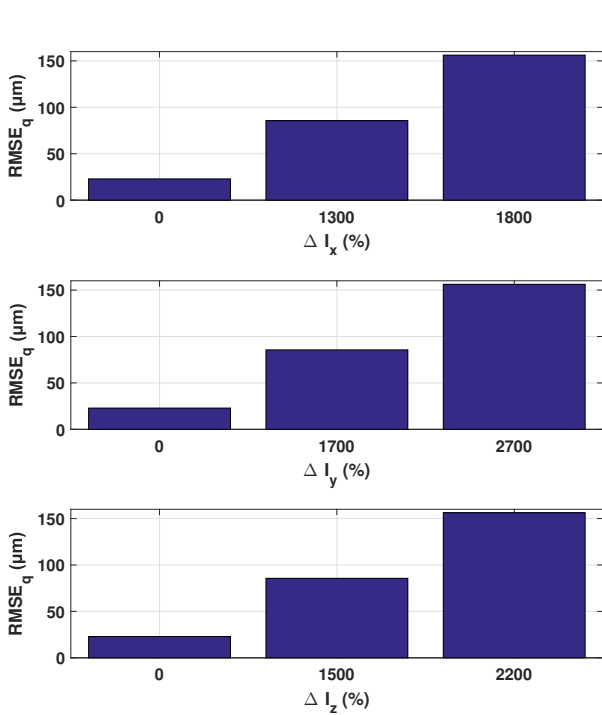


Fig. 24. Scenario 3: Evolution of the RMSE_q in joint space of the proposed controller versus the moving platform inertia uncertainties in %.

TABLE X
SCENARIO 4 (1ST TEST): TRACKING PERFORMANCE EVALUATION

Controllers	RMSE _q (μm)	RMSE _t (μm)	RMSE _r (mdeg)
SMC	67.2066	25.7547	4.0435
FFSMC	38.9397	21.2443	2.4732
AFbSMC	33.5231	18.2485	2.0547
Imp./SMC	50.12 %	29.14 %	49.18 %
Imp./FFSMC	13.91 %	14.10 %	16.92 %

25. For a better visual clarity, the plot is zoomed in within the interval [19s, 21s]. The proposed solution clearly reduces these errors, compared to the other controllers. Fig. 26 showing the Cartesian tracking errors within the interval [19s, 21s] for a readability purposes, confirms this improvement. This advantage of the proposed control solution is especially useful for applications with high dynamics in terms of velocities and accelerations, like in motion simulators. The generated motor control inputs are plotted in Fig. 27, within the range of time [19s, 21s] for better readability. The proposed control solution does not need any additional energy, compared to the other controllers, and the torque inputs remain within their admissible range. However, for high dynamics, peaks may appear in the control signals, such as the fourth motor control input Γ₄, especially for the conventional SMC scheme, which is caused by measurement noise. The RMSE performance indices, summarized in TABLEs X, XI, and XII, demonstrate the superiority of the proposed control scheme for this scenario.

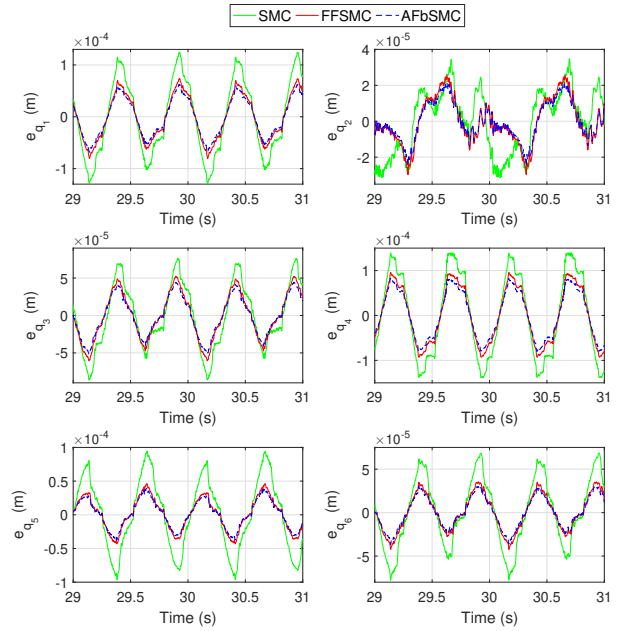


Fig. 25. Scenario 4 (3rd Test): Evolution of the joint tracking errors versus time.

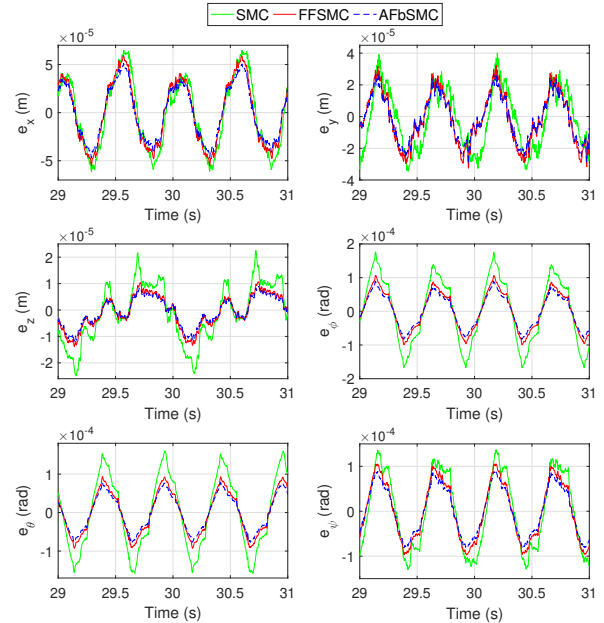


Fig. 26. Scenario 4 (3rd Test): Evolution of the Cartesian tracking errors versus time.

TABLE XI
SCENARIO 4 (2ND TEST): TRACKING PERFORMANCE EVALUATION

Controllers	RMSE _q (μm)	RMSE _t (μm)	RMSE _r (mdeg)
SMC	101.7154	33.6763	6.4124
FFSMC	63.3949	29.5045	4.1243
AFbSMC	53.6741	24.9358	3.4529
Imp./SMC	47.23 %	25.95 %	46.15 %
Imp./FFSMC	15.33 %	15.48 %	16.28 %

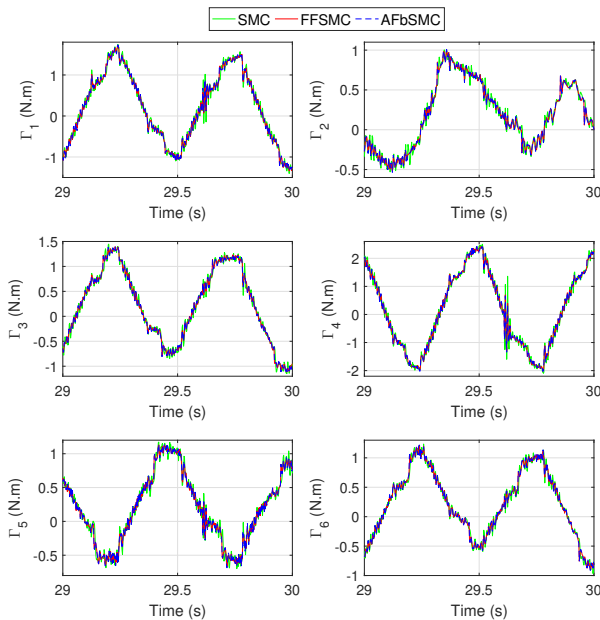


Fig. 27. Scenario 4 (3rd Test): Evolution of the input torques versus time.

TABLE XII
SCENARIO 4 (3RD TEST): TRACKING PERFORMANCE EVALUATION

Controllers	$RMSE_q(\mu m)$	$RMSE_t(\mu m)$	$RMSE_r(mdeg)$
SMC	123.9971	38.4939	7.9122
FFSSMC	77.2285	33.5279	5.1521
AFbSMC	65.7577	28.4627	4.2905
Imp./SMC	46.96 %	26.06 %	45.77 %
Imp./FFSSMC	14.85 %	15.10 %	16.72 %

V. CONCLUSION AND FUTURE WORK

In this paper, a new adaptive feedback sliding mode controller is proposed for improved tracking performance of parallel kinematic manipulators (PKMs) in different operating conditions. The MISTRAL parallel robot is used to validate the proposed control solution, which is specially designed to guarantee robustness towards uncertainties, such as additional payloads and high dynamics trajectories. To properly design the control contribution, the MISTRAL parallel robot kinematic and dynamic models are developed. The original SMC controller and the proposed one are detailed, and the stability analysis of the resulting closed-loop system is addressed. The proposed controller has been experimentally compared to the original SMC controller as well as the FFSSMC controller in different operating conditions, demonstrating clear improvements in tracking performance. It ensures nominal root mean square tracking errors of (i) about $22 \mu m$ in joint space, and (ii) about $27 \mu m$ in traveling plate Cartesian position. In future work, the proposed control solution can be augmented by dynamic parameters estimation, where the nominal feedforward term can be redesigned as adaptive. Additionally, the first-order sliding mode can be redesigned by introducing a high-order super-twisting algorithm [36].

ACKNOWLEDGMENT

This study was supported by the SYMETRIE company, within the CIFRE (Convention Industrielle de Formation par la Recherche) research project, Grant N° 2021/0900.

REFERENCES

- [1] W. Manfred and S. Dirk, "Parallel kinematic machine tools—current state and future potentials," *CIRP Annals*, vol. 51, no. 2, pp. 671–683, 2002.
- [2] G. S. Natal, A. Chemori, and F. Pierrot, "Dual-space control of extremely fast parallel manipulators: Payload changes and the 100g experiment," *IEEE Transactions on Control Systems Technology*, vol. 4, no. 23, pp. 1520–1535, 2015.
- [3] F. Raptopoulos, M. Koskinopoulou, and M. Maniadakis, "Robotic pick-and-toss facilitates urban waste sorting," in *2020 IEEE 16th International Conference on Automation Science and Engineering (CASE)*, pp. 1149–1154, IEEE, 2020.
- [4] J.-P. Merlet, *Parallel robots*, vol. 128. Springer Science & Business Media, 2006.
- [5] H. Saïed, A. Chemori, M. Bouri, M. E. Rafei, and C. Francis, "Feed-forward super-twisting sliding mode control for robotic manipulators: Application to pkms," *IEEE Transactions on Robotics*, pp. 1–18, 2023.
- [6] W. Dong, Z. Du, Y. Xiao, and X. Chen, "Development of a parallel kinematic motion simulator platform," *Mechatronics*, vol. 23, no. 1, pp. 154–161, 2013.
- [7] J. Shim, S. Song, D. Kwon, and H. Cho, "Kinematic feature analysis of a 6-degree-of-freedom in-parallel manipulator for micro-positioning surgical," in *Proceedings of the 1997 IEEE/RSJ International Conference on Intelligent Robot and Systems. Innovative Robotics for Real-World Applications. IROS '97*, vol. 3, pp. 1617–1623, 1997.
- [8] A. Chemori, "Control of complex robotic systems: Challenges, design and experiments," in *2017 22nd International Conference on Methods and Models in Automation and Robotics (MMAR)*, pp. 622–631, IEEE, 2017.
- [9] W. Shang, S. Cong, and Y. Ge, "Coordination motion control in the task space for parallel manipulators with actuation redundancy," *IEEE Transactions on Automation Science and Engineering*, vol. 10, no. 3, pp. 665–673, 2013.
- [10] G. El-Ghazaly, M. Gouttefarde, and V. Creuze, "Adaptive terminal sliding mode control of a redundantly-actuated cable-driven parallel manipulator: Cogiro," in *able-Driven Parallel Robots: Proceedings of the Second International Conference on Cable-Driven Parallel Robots*, pp. 179–200, Springer, 2015.
- [11] B. Dasgupta and T. Mruthyunjaya, "The stewart platform manipulator: a review," *Mechanism and Machine Theory*, vol. 35, no. 1, pp. 15–40, 2000.
- [12] H. D. Taghirad, *Parallel robots: mechanics and control*. CRC press, 2013.
- [13] Y. Pan and F. Gao, "Mechanism topology design for novel parallel-parallel hexapod robot," in *2014 UKACC International Conference on Control (CONTROL)*, pp. 737–742, IEEE, 2014.
- [14] S. Staicu, *Dynamics of Parallel Robots*. Springer, 2019.
- [15] E. Idà, T. Bruckmann, and M. Carricato, "Rest-to-rest trajectory planning for underactuated cable-driven parallel robots," *IEEE Transactions on Robotics*, vol. 35, no. 6, pp. 1338–1351, 2019.
- [16] M. R. J. Harandi, A. Hassani, M. I. Hosseini, and H. D. Taghirad, "Adaptive position feedback control of parallel robots in the presence of kinematics and dynamics uncertainties," *IEEE Transactions on Automation Science and Engineering*, pp. 1–11, 2023.
- [17] M. G. Villarreal-Cervantes and J. Alvarez-Gallegos, "Off-line pid control tuning for a planar parallel robot using de variants," *Expert Systems with Applications*, vol. 64, pp. 444–454, 2016.
- [18] A. Al-Mayyahi, A. Aldair, and C. Chatwin, "Control of a 3-rrr planar parallel robot using fractional order pid controller," *International Journal of Automation and Computing*, vol. 17, p. 822–836, 2020.
- [19] Y. Su, D. Sun, and C. Zheng, "Nonlinear trajectory tracking control of a closed-chain manipulator," in *Fifth World Congress on Intelligent Control and Automation (IEEE Cat. No.04EX788)*, vol. 6, pp. 5012–5016, 2004.
- [20] G. Hassan, A. Chemori, L. Chikh, P.-E. Hervé, M. El Rafei, C. Francis, and F. Pierrot, "Rise feedback control of cable-driven parallel robots: Design and real-time experiments," in *Proceedings of the International Conference on Control Applications*, vol. 52, pp. 8519–8524, Elsevier, 2020.

- [21] H. Saied, A. Chemori, M. Bouri, M. El Rafei, C. Francis, and F. Pierrot, "A new time-varying feedback rise control for second-order nonlinear mimo systems: theory and experiments," *International Journal of Control*, vol. 94, no. 8, pp. 2304–2317, 2021.
- [22] M. Ghafarian Tamizi, A. A. Ahmadi Kashani, F. Abed Azad, A. Kalhor, and M. T. Masouleh, "Experimental study on a novel simultaneous control and identification of a 3-dof delta robot using model reference adaptive control," *European Journal of Control*, vol. 67, p. 100715, 2022.
- [23] M. Bennehar, A. Chemori, and F. Pierrot, " \mathcal{L}_1 adaptive control of parallel kinematic manipulators: Design and real-time experiments," in *2015 IEEE International Conference on Robotics and Automation (ICRA)*, pp. 1587–1592, IEEE, 2015.
- [24] H. Jabbari Asl and F. Janabi-Sharifi, "Adaptive neural network control of cable-driven parallel robots with input saturation," *Engineering Applications of Artificial Intelligence*, vol. 65, pp. 252–260, 2017.
- [25] W.-W. Shang and S. Cong, "Nonlinear computed torque control for a high-speed planar parallel manipulator," *Mechatronics*, vol. 19, no. 6, pp. 987–992, 2009.
- [26] W. W. Shang, S. Cong, Z. X. Li, and S. L. Jiang, "Augmented nonlinear pd controller for a redundantly actuated parallel manipulator," *Advanced Robotics*, vol. 23, no. 12–13, pp. 1725–1742, 2009.
- [27] I. T. Pietsch, M. Krefft, O. T. Becker, C. C. Bier, and J. Hesselbach, "How to reach the dynamic limits of parallel robots? an autonomous control approach," *IEEE Transactions on Automation Science and Engineering*, vol. 2, no. 4, pp. 369–380, 2005.
- [28] B. Zhou, Y. Wang, B. Zi, and W. Zhu, "Fuzzy adaptive whale optimization control algorithm for trajectory tracking of a cable-driven parallel robot," *IEEE Transactions on Automation Science and Engineering*, pp. 1–12, 2023.
- [29] Y. Yun and Y. Li, "Active vibration control based on a 3-dof dual compliant parallel robot using lqr algorithm," in *2009 IEEE/RSJ International Conference on Intelligent Robots and Systems*, pp. 775–780, IEEE, 2009.
- [30] J. C. Santos, M. Gouttefarde, and A. Chemori, "A nonlinear model predictive control for the position tracking of cable-driven parallel robots," *IEEE Transactions on Robotics*, vol. 38, no. 4, pp. 2597–2616, 2022.
- [31] M. Jafarinasab, M. Keshmiri, H. Azizan, and M. Danesh, "Sliding mode control of a novel 6-dof parallel manipulator with rotary actuators," in *2011 16th International Conference on Methods & Models in Automation & Robotics*, pp. 218–223, IEEE, 2011.
- [32] D. Stewart, "A platform with six degrees of freedom," *Proceedings of the institution of mechanical engineers*, vol. 180, no. 1, pp. 371–386, 1965.
- [33] H. B. Guo and H. R. Li, "Dynamic analysis and simulation of a six degree of freedom stewart platform manipulator," *Proceedings of the Institution of Mechanical Engineers, Part C: Journal of Mechanical Engineering Science*, vol. 220, no. 1, pp. 61–72, 2006.
- [34] E. Idà, S. Briot, and M. Carricato, "Identification of the inertial parameters of underactuated cable-driven parallel robots," *Mechanism and Machine Theory*, vol. 167, p. 104504, 2022.
- [35] W. Khalil and E. Dombre, "Modeling, identification and control of robots," *Applied Mechanics Reviews*, vol. 56, pp. B37–B38, 05 2003.
- [36] Y. Shtessel, C. Edwards, L. Fridman, and A. Levant, *Sliding Mode Control and Observation (Control Engineering Series)*. Springer, 2014.
- [37] V. Santibañez and R. Kelly, "Pd control with feedforward compensation for robot manipulators: analysis and experimentation," *Robotica*, vol. 19, no. 1, p. 11, 2001.
- [38] M. Bennehar, G. El-Ghazaly, A. Chemori, and F. Pierrot, "A novel adaptive terminal sliding mode control for parallel manipulators: Design and real-time experiments," in *2017 IEEE International Conference on Robotics and Automation (ICRA)*, pp. 6086–6092, IEEE, 2017.
- [39] M. Escorcia-Hernández, Jonatan, A. Chemori, and H. Aguilar-Sierra, "Adaptive rise feedback control for robotized machining with pkms: Design and real-time experiments," *IEEE Transactions on Control Systems Technology*, vol. 31, no. 1, pp. 39–54, 2023.
- [40] F. Plestan, Y. Shtessel, V. Bregeault, and A. Poznyak, "New methodologies for adaptive sliding mode control," *International journal of control*, vol. 83, no. 9, pp. 1907–1919, 2010.
- [41] H. Saied, *On Control of Parallel Robots for High Dynamic Performances: From Design to Experiments*. PhD thesis, Université de Montpellier, 2019.



Youcef Fitas received the M.Eng. degree and M.Sc. degree in automation engineering from the National Polytechnic School of Constantine (ENPC) Constantine, Algeria, in 2020. He is actually a Ph.D. student in robotics at the Montpellier Laboratory of Informatics, Robotics, and Microelectronics, Montpellier, France. Also, he is currently working as R&D engineer with the company SYMETRIE, Nîmes, France. His main research interests include advanced control of parallel robotics.



Ahmed Chemori received the M.Sc. and Ph.D. degrees both in automatic control from the Grenoble Institute of Technology, Grenoble, France, in 2001 and 2005, respectively. He has been a Postdoctoral Fellow with the Automatic Control Laboratory, Grenoble, France, in 2006. He is currently a tenured Research Scientist in automatic control and robotics with the Montpellier Laboratory of Informatics, Robotics, and Microelectronics. His research interests include nonlinear, adaptive, and predictive control and their applications in robotics.



Johann Lamaury received the M.Eng. degree in mechatronics engineering from the Institut National des Sciences Appliquées (INSA) and the M.Sc. in control and robotics from the Télécom Physique Strasbourg school, Strasbourg, France, in 2010. He received the Ph.D. degree in robotics at the Montpellier Laboratory of Informatics, Robotics, and Microelectronics, Montpellier, France, in 2013. He is currently working as the software engineering manager with the company SYMETRIE, Nîmes, France. His main research interests include advanced

control of parallel robotics.



Thierry Roux received the M.Eng. degree in mechanical engineering from the ITII - ENSAM Aix en Provence, France, in 1999. He is a co-founder of the company SYMETRIE, Nîmes, France, in 2001. Currently, he is working as technical director at this company. His main research interests on parallel robotics, especially in metrology, resolution, and advanced control.